Effect of Surfactants on the Structural and Magnetic Properties of NiFe$_2$O$_4$ Nanoparticles

P. Priyadharshini[iD], K. Pushpanathan[*,iD] and V. Kathiravan[iD]

Department of Physics, Government Arts College (Bharathidasan University), Karur-639005, India

*Corresponding author: E-mail: kpngackr@gmail.com

In present work, nickel ferrite magnetic nanoparticles were synthesized by simple precipitation method using different surfactants and the effect of surfactants on its structural and magnetic properties have been studied. Average crystallite size calculated from Scherrer formula is in the range of 20-51 nm. Fourier transform infrared spectra confirmed the tetrahedral and octahedral vibrational bands at 400 and 650 cm^{-1}, respectively. The UV-visible absorbance spectra confirmed that the direct bandgap of nickel ferrite between 3.48 and 3 eV for different surfactants. Transmission electron microscope analysis validated the establishment of single-phase nickel ferrite nanoparticles in the range of ~19-51 nm. Saturation magnetization varies with surfactants between 28.6 and 50.3 emu/g, 76 to 95 Oe and 2.19 to 6.07 emu/g, respectively. The superparamagnetic nature of the samples is supported by the low coercivity (< 100 Oe).

Keywords: Nickel ferrite, Capping agent, Crystal structure, Superparamagnetism.

INTRODUCTION

Ferrites are a wide family of complicated, technologically important magnetic oxides. Depending on their crystal structure and cation distribution, they are categorized as (i) spinel and (ii) inverse spinel ferrites with the collective molecular prescription MFe$_2$O$_4$, here M is a divalent metal cation (M = Mn, Co, Ni, Cu, Fe, Zn). The spinel ferrite is a face-centered cubic (FCC) lattice made of oxygen ions with the space group Fd$\overline{3}$m. Further, they consist of 32 oxygen atoms in an FCC lattice, in which the metal ions are divided into eight tetrahedral (A) sites and 16 octahedral (B) sites [1]. Their unique electrical and magnetic characteristics depend on the ion composition, its charges and its distribution between tetrahedral sites (A) and octahedral sites (B). Ferrite nanomaterials are gathering attention in various technological fields, including high-density storage devices, microwave devices, recording tapes, telecommunication devices, drug delivery systems, magnetic cell separation and magnetic resonance imaging [2].

Over the past decades, NiFe$_2$O$_4$ attracted continuous interest among the various ferrites owing to their outstanding structural, optical, magnetic, thermal, catalytic and chemical properties. It may be a ferro or ferrimagnetic material with high intrinsic resistivity, low coercivity, low dielectric and magnetic losses,

strong chemical stability and mechanical strength with high curie temperatures to maintain the magnetic characteristics. Nanocrystalline nickel ferrite is a superparamagnetic material, and it exhibits an inverse spinel cubic structure. Each unit cell of nanosized NiFe$_2$O$_4$ contains eight units of NiFe$_2$O$_4$. Half of the ferric ions occupy the tetrahedral sites (A-sites), while the other half of the ferric ions occupy the octahedral sites (B-sites). As a result, the compound can be represented by the formula (Fe^{3+})$_A$[Ni^{2+}Fe^{3+}]$_B$O$_4^{2-}$, where A and B stand for tetrahedral and octahedral sites, respectively.

Several chemical processes have been developed for the synthesis of nickel ferrite nanoparticles, including hydrothermal method [3], sol-gel method [4], thermal decomposition method [5], mechanochemical method [6], ball milling method [7] and co-precipitation method [8]. Among these various synthesis techniques, co-precipitation method gains much attention because of its advantages, like economic, simple, easy reproducibility, shorter time, particle size and shape control and the ability to obtain large quantities of NiFe$_2$O$_4$ nanoparticles. Apart from that the precipitation method gives up smaller nanoparticles compared to sol-gel and hydrothermal methods.

The surfactant plays an important role in controlling the shape and size of the nanoparticles due to its influence on nucle-

ation and growth kinetics. Furthermore, due to interparticle magnetic interactions, magnetic nanoparticles have a robust tendency to agglomerate. To prevent such agglomeration, magnetic nanoparticles (MNPs) are typically coated with a polymer to keep them suspended and prevent any reaction with atmospheric oxygen. The magnetic nanoparticles are commonly coated with a surfactant, also called a capping agent, which plays the dual role of controlling the grain growth and avoiding agglomeration while promoting suspension [9]. Therefore, the choice of the surfactant and its appropriate amount are important for tailoring the size and morphology of magnetic nano-particles in the precipitation method [10]. When a cationic surfactant with a hydrophilic head and a hydrophobic tail is added to a solution, reverse micelles form. Keeping aqueous ions inside these micelles may be an efficient technique for regulating particle nucleation and growth. Because of the presence of surfactant, the surface tension of the solution is reduced, lowering the energy required for the formation of the new phase [11]. However, identifying a simple method for obtaining pure, ultrafine and homogeneous nickel ferrite nano-structures is a serious challenge for materials scientists.

A literature survey reveals that several researchers are studying the effects of surfactant-assisted ferrite nanoparticles like CTAB, oleic acid, PVA, PEG, PVP, SDS, *etc.*, on their structural, optical, and magnetic properties. For instance, Sonia *et al.* [12] showed that the surfactants PVB, EDTA, CTAB control the size of NiFe₂O₄ nanoparticles and thus noticeably influence the magnetic parameter. Likewise, Sivakumar *et al.* [13] prepared nickel ferrite magnetic nanoparticles using poly-vinyl alcohol (PVA) as a surfactant through the sol-gel auto combustion method. They also reported that PVA is an efficient fuel to get the spherical and smaller magnetic nanoparticles. Baykal *et al.* [14] reported the CTAB assisted hydrothermal synthesis and studied the magnetic properties of $Ni_xCo_{1-x}Fe_2O_4$ nanoparticles ($x = 0.0, 0.6, 1.0$). They found high phase purity and crystallinity in the synthesized samples and the suitability of them for magnetic recording applications [14]. Asiri *et al.* [15] have fabricated the NiFe₂O₄ nanoparticles at 900, 1000 and 1100 ºC *via* the sol-gel route using citric acid and they found an increase in saturation magnetization and magnetic moment of the uniaxial NiFe₂O₄ nanoparticles . Iranmanesh *et al.* [16] investigated the magnetic stuff of Ni ferrite nano-particles with diameters of less than 10 nm, synthesized by a one-step co-precipitation route at diverse pH values without a capping agent. They reported that NiFe₂O₄ nanoparticles are indirect bandgap materials whose bandgap upturns with pH value (2.41-2.53 eV) due to the establishment of bigger particles with condensed surface effects.

In this work, we reported the synthesis of NiFe₂O₄ nano-particles *via* a co-precipitation method without and with diffe-rent surfactants, namely, polyethylene glycol (PEG), cetyl-trimethyl ammonium bromide (CTAB), polyvinyl alcohol (PVA) and oleic acid (OA). Analytical techniques, such as X-ray diffractometer, fourier transform infrared spectroscopy, trans-mission electron microscopy, electron spin resonance spectro-scopy and so on, were used to look at the samples that had been prepared.

EXPERIMENTAL

Synthesis: The surfactant-free and surfactant-assisted NiFe₂O₄ nanoparticles were prepared by the co-precipitation method using analytical grade nickel chloride hexahydrate (NiCl2.6H2O, purity 99.5%, Sigma-Aldrich, USA), iron(III) chloride hexahydrate (FeCl₃·6H₂O, purity 99.5%, Sigma-Aldrich) with ammonia hydroxide (NH₄OH) as precipitating agent and polyethylene glycol (PEG), cetyltrimethylammonium bromide (CTAB), oleic acid (OA) and polyvinyl alcohol (PVA) as surfactants. All the chemicals have been used not having further purification. The beakers and other glass items were washed many times with acetone. Double distilled water was used as a solvent and ethanol for washing.

The stoichiometric amounts of reactants for NiCl₃·6H₂O and FeCl₃·6H₂O were used. Every salt was dissolved in 125 mL deionized water with constant stirring, then mixed together and heated to 60 ºC on a hot-plate for 10 min. The aqueous solution has been then magnetically agitated for around 30 min to produce a homogeneous, pure, yellow stock solution. It was divided into five parts that were roughly equal in quantity. To make surfactant-free NiFe₂O₄ nanoparticles, a diluted NH₄ solution was mixed with one part of the above-mentioned yellow stock solution dropwise until the pH reached 12. After being under ultrasonic radiation for 30 min at room tempera-ture, the homogeneous solution was stirred for 3 h at 80 ºC. Within this 3 h duration, the intermediate hydroxides transform into spinal ferrite. At this stage, the solution colour changed and a precipitate developed, indicating that the compound was formed. Then the final solution was allowed to cool to room temperature and allowed to precipitate for three days. A bar magnet has been used to assemble the dark brown magnetic particles that accumulated at the lower-most of the beaker. The precipitate has been then carried away multiple times with ethanol and distilled water till the pH of the solution was decreased to seven to eliminate traces of chloride ions, nitrogen, unreacted chemicals and undesirable contami-nants and then filtered [17]. For every wash, the magnetic nano-particles were collected from the bottom using a bar magnet, which allows the filtrates to float and be empty. The precipitates was then centrifuged for 2 min at 800 rpm and then dehydrated at 100 ºC in a hot air oven for 14 h to eliminate water content. To end with, the product was crushed into a fine powder in an agate mortar. Following this, all the powders were annealed at 800 ºC for 2 h to get good crystallites. The following unbalanced chemical reaction is thought to be responsible for the formation of NiFe₂O₄:

$$NiCl_2 \cdot 6H_2O + FeCl_3 \cdot 6H_2O + NH_3 \cdot nH_2O \longrightarrow$$
$$NiFe_2O_4 + NH_4Cl + N_2 + H_2O\uparrow$$
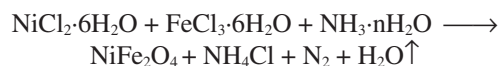
This surfactant-free NiFe₂O₄ sample was labeled as NSF. For the synthesis of surfactant-covered NiFe₂O₄ samples, a specific amount of oleic acid, CTAB, PEG, and PVA were added to the above yellow stock solution as surfactants before adding the diluted NH₄ solution. Other procedures were the same as those for the surfactant-free sample. Hereafter, the surfactant-free, PEG capped, CTAB capped, PVA capped and

oleic acid capped $NiFe_2O_4$ nanopowders were labeled as NSF, NPEG, NCTAB, NPVA and NOA, respectively.

Characterization: The synthesized $NiFe_2O_4$ nanoparticles were considered for unit cell parameters, compositional, nano-structural, photosensitive and magnetic characterization. The unit cell parameters of the as-prepared $NiFe_2O_4$ nanopowders were carried out by scrutinizing the X-ray diffraction (XRD) patterns documented by a Philips X′pert diffractometer emp-loyed with $CuK\alpha$ radiation ($\lambda = 1.54056$ Å) in the angle range of $2\theta = 10$-$80°$ at a scan rate of $0.05°/s$ functioned at an working voltage of 40 kV/30 mA. The optical absorption spectra of the nanoparticles were recorded using PG Instruments Ltd. T80 UV-Vis spectrometer in the wavelength range of 190-1100 nm was used to explore their optical features. The fourier transform infrared (FTIR) spectra of the samples were obtained using a Thermo Scientific Nicolet iS10 spectrometer (MERCK Ltd.) in the wavenumber region 4000-400 cm^{-1} to examine their octahedral and chemical properties in a better way. The samples were morphologically characterized using high-resolution transmission electron microscope (HR-TEM) Zeiss EM10 TEM equipment with an ultra-high-resolution pole piece working at an accelerating voltage of 300 kV. Composition analysis was done with the help of a Bruker (QUANTAX EDS) elemental analyzer. The magnetic characteristics of the samples were inves-tigated using a vibrating sample magnetometer (Lakeshore VSM 7410) between the magnetic field + 1.6 KOe and -1.6 KOe at room temperature to obtain the saturation magnetization, coercivity, retentivity and other magnetic parameters.

RESULTS AND DISCUSSION

XRD studies: Fig. 1 depicts the X-ray diffraction (XRD) pattern of $NiFe_2O_4$ nanoparticles synthesized without and with surfactants (PEG, CTAB, PVA and oleic acid), whose diffraction peaks were observed at around 18.37°, 30.30°, 35.68°, 37.37°, 43.38°, 53.80°, 57.32°, 62.97°, 63.10° and 74.61° corresponding to the crystal planes (111), (220), (311), (222), (400), (422), (511) and (440), respectively.
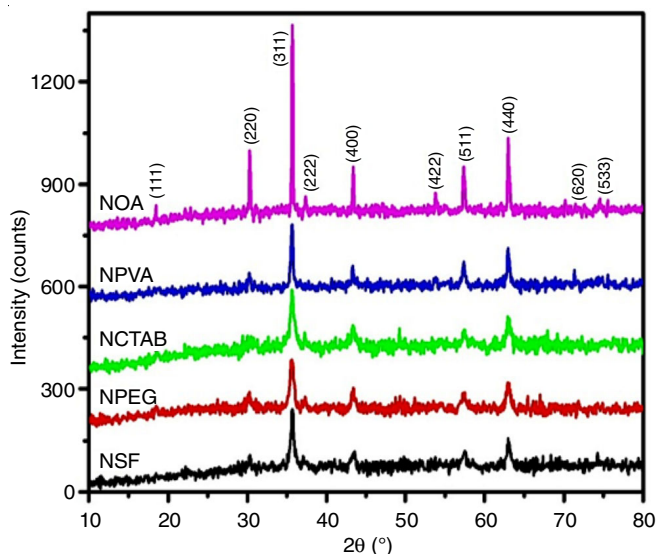

Fig. 1. X-ray diffraction patterns of $NiFe_2O_4$ samples synthesized using various capping agents recorded at room temperature

The diffraction peaks of all five samples were analyzed with X′pert high score software and then compared with the standard JCPDS data card No. 89-4927. By doing so, it was found that the obtained results are in good compromise with the reported values of the JCPDS data card (No.89-4927), which confirms the formation of single-phase inverse spinel $NiFe_2O_4$ nanoparticles. The XRD pattern further confirms the FCC structure of the samples. Moreover, the absence of diffraction peaks at 33.2°, 49.5°, 66.2° and 72.1° confirmed that the synthesized samples are free from the contamination phase of α-Fe_2O_3 and NiO within the limit of X-ray detection [18]. The broadness of the peaks confirmed the nanoscale range of crystallites and the multiple peaks confirmed the polycrys-talline nature of the samples. In comparison, the XRD peaks of oleic acid coated $NiFe_2O_4$ sample (NOA) are sharper than the others, which imply that oleic-acid improved the crystallinity of $NiFe_2O_4$ nanoparticles. It may be due to the fact that the growth rate of particles in the NOA sample is faster and the nucleation rate is slower, resulting in a higher degree of crystall-inity. Due to a decrease in crystallinity, broadening of diffraction peaks occurred in other samples such as NSF, NPEG, NCTAB, and NPVA samples. This indicates that the surfactant has a considerable influence on the nucleation and growth rates, which in turn controls the crystallite size, meaning that nucle-ation rate is larger in NSF, NPEG, NCTAB, and NPVA samples than the growth rate [19]. The rough estimation of average crystallite size (D) was done from the strongest peak of (311), using Scherrer's formula as given here [20].

$$D \ (nm) = \frac{0.9\lambda}{\beta\cos\theta}$$

where λ denotes the wavelength (1.541 Å) of the X-ray ($CuK\alpha$) radiation, β represents the full-width at half maximum (FWHM) and θ signifies the Bragg's diffraction angle. The estimated mean crystallite sizes of NSF, NPEG, NCTAB, NPVA and NOA samples were 23.5, 19.1, 22.2, 35.8, and 52.6 nm, respectively. Likewise, Baykal *et al.* [21] also obtained the crystalline size of nickel ferrite nanoparticles in the range of 15-55 nm.

Strain is the deformation experienced by a material that undergoes stress. The deformation occurs on a micro-level for micro-strain effects. The microstrain (ε) [22] for uncapped and capped ferrite nanoparticles was calculated as.

$$\varepsilon = \frac{\beta\cot\theta}{4}$$

Microstrain calculation shows that the strain of NSF, NPEG, NCTAB, NPVA and NOA samples is 0.0034, 0.0069, 0.0041, 0.0030 and 0.0021, respectively. The highest strain, 0.0069 of NOA sample, is due to the faster growth rate and the larger crystallite size. On the other hand, the surfactants PEG, CTAB and PVA control and stabilize the $NiFe_2O_4$ nanoparticles from reduction-oxidation processes and redissolution, which leads to a decrease in strain in samples NSF, NPVA and NOA (Table-1) [23].

Estimation of crystallite size using Scherrer's formula includes the microstrain, which is developed during the synthesis process. The W-H plot method gives the average crystallite size

TABLE-1
STRUCTURAL PARAMETERS OF NiFe$_2$O$_4$ NANOPARTICLES WITHOUT AND WITH CAPPING AGENTS

Sample code	Crystallite size (D) nm		Micro-strain (ε)	Lattice constant (a) Å	Dislocation density ($\delta \times 10^{10}$ lines/cm^2)	Volume of the nanoparticles (V) (a')^{3}Å^3	Unit cell volume (v) based on (a') Å^3
	Scherrer method (D)	W-H Plot (D')					
NSF	23.5	27.2	0.0034	8.3416	13.5	10540959	577.7
NPEG	19.1	19.5	0.0069	8.3623	26.3	3883982	579.7
NCTAB	22.2	21.6	0.0041	8.3368	21.4	5278793	578.1
NPVA	35.8	33.4	0.0030	8.3543	8.96	19516988	582.4
NOA	52.6	54.0	0.0021	8.3442	3.43	82481143	580.4

by excluding the microstrain, it is believed that the W-H method is more accurate than the Scherrer's method to calculate the crystallite size (Table-1). Hence, to estimate the crystallite size in a precise manner, the Williamson-Hall (W-H) plot was used, which is given by the equation:

$$\beta_{hkl} \cos \theta = \frac{k\lambda}{D'} + 4\varepsilon' \sin \theta$$

where the term β represents the measured FWHM in radians, θ is the Bragg angle of the diffraction peak, λ is the X-ray wavelength, D' is the effective crystallite size, and ε' is the effective microstrain calculated from the W-H method. A graph is drawn by concerning 4sin θ along the x-axis and β_{hkl}cos θ along the y-axis (Fig. 2). The peaks were fitted with a Gaussian function, and the resulting uncertainties were noted in the peak widths [24]. The average crystallite sizes thus estimated from the W-H method were 27.2, 19.5, 21.6, 33.4, and 54.0 nm for NSF, NPEG, NCTAB, NPVA and NOA samples, respectively. The crystallite sizes calculated from the W-H method are nearly the same as those of Scherrer's method. The experimental lattice constant 'a' was calculated from the XRD data using the formula:

$$\sin^2 \theta = \frac{\lambda^2 (h^2 + k^2 + l^2)}{4a^2}$$

where (hkl) represents the miller indices, θ represents the diffraction angle, and λ represents the wavelength of X-ray beam used. The lattice constants thus calculated are 8.3416 Å, 8.3623 Å, 8.3368 Å, 8.3543 Å and 8.3442 Å for the samples NSF, NPEG, NCTAB, NPVA and NOA, respectively. The calculated lattice constants are slightly higher than the lattice constant of bulk NiFe$_2$O$_4$ (8.339 Å) reported in the JCPDS card No: 44-1485. The dislocation density (δ) is the measure of the length of dislocation per unit volume (number of defects). It is a measure of the defects in the crystalline samples, which can be obtained from the relationship:

$$\delta = \frac{1}{(D')^2}$$

where 'D''' is the average crystallite size determined by the W-H method. These values gradually increased with the decrease in for NSF and NPEG samples, and then they decreased, which indicates that lattice imperfection decreases with the crystallite size. The lower dislocation density of NOA sample is reliable with the larger crystallites, which has better crystallinity. The uncapped and surfactant-capped NiFe$_2$O$_4$ nanoparticles exhibit a cubic system, for which the volume (v) of the unit cell was calculated using the equation given below:

Fig. 2. W-H plots of NiFe$_2$O$_4$ ferrite magnetic nanoparticles synthesized using different capping agents

$$v = (a')^3$$

If 'v' is the volume of a nanoparticle, by assuming the majority of the particles are spherical in shape, then its volume can be calculated by using the following formula:

$$V = \frac{4}{3} \pi \left(\frac{D'}{2} \right)^3$$

Furthermore, the ratio of V to v gives the number of unit cells (η) contained in a grain and it is determined using the equation below:

$$\eta = \left(\frac{V}{v} \right) = \frac{0.6 \, (D')^3}{(a')^3}$$

In the cubic lattice, the average bond lengths present between cation and anion ions can be calculated using the relationship $r = 0.583a'$, where 'a'' is the true lattice constant obtained from the Nelson-Riley method. Bond lengths obtained from this
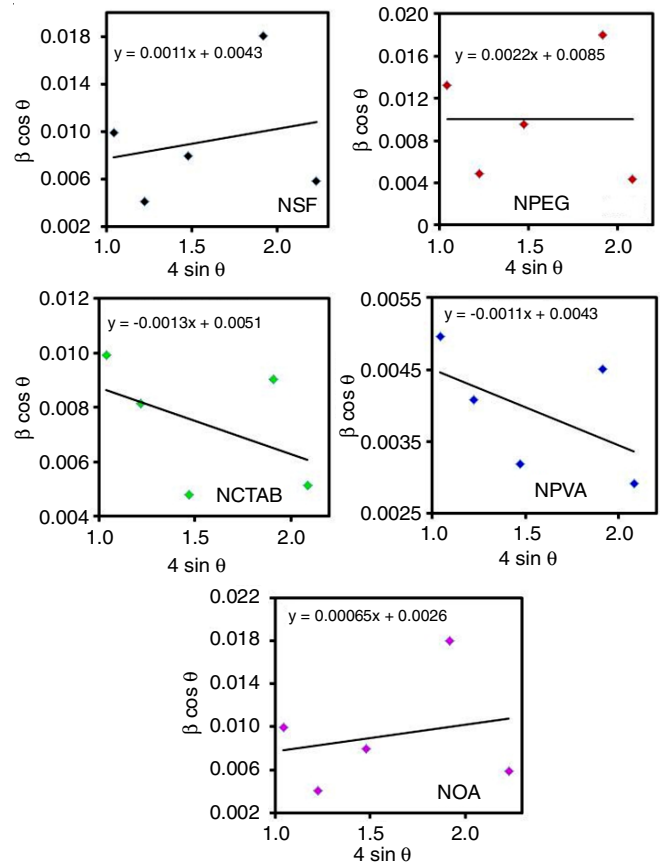
relationship were 4.8556 Å, 4.8612 Å, 4.8567 Å, 4.8687 Å and 4.8631 Å for surfactant free (NSF), polyethylene capped (NPEG), CTAB capped (NCTAB), PVA capped (NPVA), and oleic acid capped (NOA) NiFe$_2$O$_4$ nanoparticles, respectively.

FTIR studies: The FTIR spectra of the synthesized nickel ferrite samples are shown in Fig. 3. The broad absorption peak observed around 3443 cm^{-1} is ascribed to the stretching vibration mode of the O-H group of absorbed water molecules by the KBr pellet [25]. The small intense peaks at 2936 cm^{-1} and 2923 cm^{-1} in NPEG, NCTAB and NPVA samples are due to the symmetric and asymmetric stretching bands of the C-H group, respectively, whereas NSF and NOA samples show no presence of –CH stretching in the spectra.
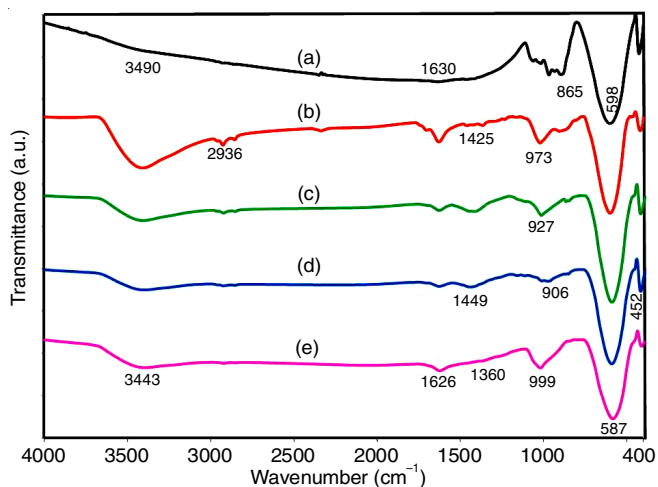

Fig. 3. FTIR spectra of (a) NSF, (b) NCTAB, (c) NPEG, (d) NPVA and (e) NOA nickel ferrite nanoparticles

It is also observed that the carboxylate C=O stretching band is slightly varied from 1630 cm^{-1} to 1626 cm^{-1} and the C–O stretching band varied between 1425 cm^{-1} and 1449 cm^{-1} in the NPEG, NPVA and NOA samples, which are the characteristics of the symmetric ν_s(COO$^-$) and asymmetric ν_{as}(COO$^-$) stretching. A combination of the molecules bound uniformly and molecules attached at such an angle to the surface accounts for the carboxylic acid bonding pattern on the exteriors of the nanoparticles [26]. Also, the attraction between the metal atom and carboxylate head is categorized into four types, such as ionic interaction, chelating (bidentate), bridging (bidentate), and monodentate [27]. The wavenumber separation (Δ) between the ν_s(COO$^-$) and ν_{as}(COO$^-$) IR bands can be used to distinguish the type of interaction between the carboxylate head and the metal atom. The largest Δ (200-320 cm^{-1}) correspond to the monodentate interaction, and the smallest Δ (<110 cm^{-1}) was for the chelating bidentate. The medium range Δ (140-190 cm^{-1}) was for the bridging bidentate. For NPEG sample, the Δ is 201 cm^{-1} (1626-1425) while for NOA it is 222 cm^{-1} (1648-1426). They are ascribed to monodentate interaction where one metal ion is binding with one carboxylic oxygen atom. However, in the case of NPVA sample, the Δ (1631-1449= 182 cm^{-1}) was ascribed to the bridging bidentate where two metal ions are bound with two carboxylic oxygen atom. The peak at 1027-1022 cm^{-1} is assigned to O-H bending

vibrations of synthesized nickel ferrite nanoparticles [28]. There is also some PEG, CTAB, PVA and OA residues found in the particles. This is confirmed by the appearance of peaks at 999, 973, 927,906 and 973 cm^{-1} in the spectra as well. The two main vibrations of metal ions in the crystal lattice are usually observed in the range of 1000-400 cm^{-1}. The highest peak is generally observed in the range of 650-580 cm^{-1} and the lowest peak in the range of 460-400 cm^{-1} corresponds to intrinsic stretching vibrations of metal ions in the tetrahedral and octahedral sites. The tetrahedral stretching frequency is observed at 587-598 cm^{-1} confirms the exchange of Ni^{2+} and Fe^{2+} ions in the octahedral site and Fe^{3+} in the tetrahedral site. There will be an exchange of Fe^{2+} and Ni^{2+} ions in the tetrahedral sites and Fe^{3+} in the tetrahedral sites.

UV-Vis studies: Fig. 4 demonstrates the results of UV-vis spectroscopy that was used to investigate the energy gap of NiFe$_2$O$_4$ nanoparticles synthesized without and with different capping agents. The energy gap of the nanoparticles is affected by a variety of factors, such as crystalline size, dopant concentration, surface roughness and oxygen deficiency. Two opposing forces influence the bandgap of nanomaterials for example, (i) the quantum size effect causes a blue shift as the particle size decreases, while the surface and interface effect caused a red-shift in the bandgap energy as the particle size increases [29]. The peak absorption of the NPEG sample was recorded at 360 nm, and the same was also recorded at 369, 389, 395, and 400 nm for NCTAB, NSF, NPVA and NOA samples, respectively. The respective energy gap (E$_g$) was calculated using the following relation:

$$E_g \ (eV) = \frac{hc}{\lambda_{max}}$$

where, h denotes Planck's constant (6.626 × 10^{-34} J s), C is the speed of light in air or vacuum (3 × 10^8 m/s), and λ_{max} is the peak absorption of samples. The energy gap was found to be 3.44, 3.36, 3.19, 3.14, and 3.10 eV for NPEG, NCTAB, NSF, NPVA and NOA samples, respectively. The measured optical band gap is very similar to the value as stated by Rahman *et al.* [30].
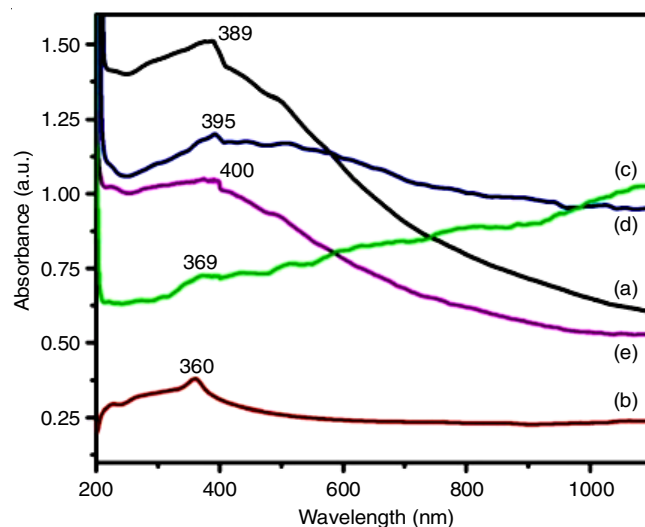

Fig. 4. Optical absorbance spectra of (a) NSF, (b) NCTAB, (c) NPEG, (d) NPVA and (e) NOA NiFe$_2$O$_4$ nanoparticles

The difference in bandgap of the synthesized ferrite nanoparticles can be attributed to changes in structural parameters such as crystalline size, defects and morphology, all of which have a strong impact on absorption properties. In addition, the refractive index of all $NiFe_2O_4$ nanoparticles were also calculaed using the optical energy bandgap. The refractive index (η) is an important parameter in decisive the optical and electrical possessions of semiconducting magnetic nanoparticles and for the design of hetero-structured lasers for optoelectronic devices and solar cells [31].

Microstructural studies: Nickel ferrite nanoparticles synthesized with four different surfactants such as PEG, PVA, CTAB and OA and surfactant free (NSF) samples have been morphologically studied using TEM (Figs. 5 and 6). The particle size and interplanar spacing were calculated using Image J software and the rings of the SAED pattern were indexed based on the data obtained from the Image J analysis. A sample synthesized using PEG showed almost spherical nanoparticles of monomodal distribution. From the measurements of TEM micrographs (Fig. 5), an average particle size calculated to be 18.7 ± 2.1 nm. The smallest particle size of NPEG sample among the other samples is due to the property of PEG, which slows down the reaction and precipitation process. The particles of the sample coated with CTAB (Fig. 6) show severe agglomeration with various morphologies (including a nano-rod) with varying particle sizes from 5 to 30 nm, indicating that due to a lack of surfactant (which functions as a capping agent), the nucleated particles begin to develop at random.
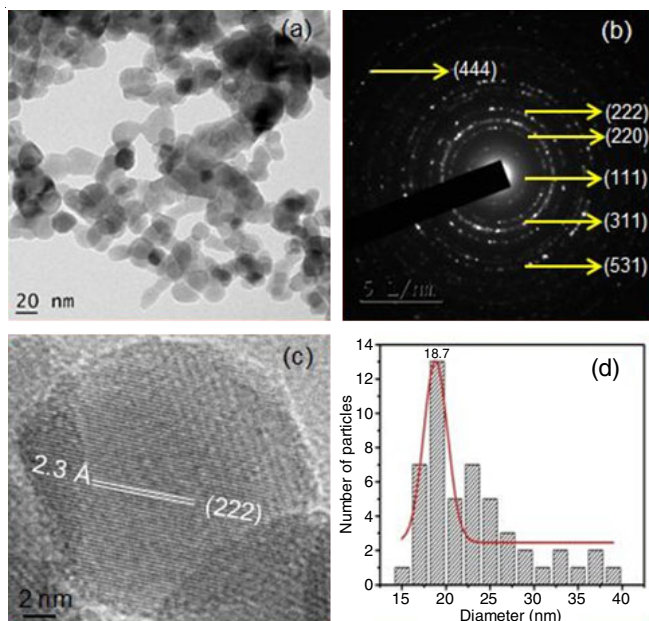

Fig. 5. Microstructural information of NPEG sample; (a) TEM image, (b) corresponding SAED pattern, (c) HR-TEM image of (222) lattice plane and (d) particle size distribution plot

Fully coated nickel ferrite nanoparticles grew uniformly, resulting in a spherical shape, whereas unprotected particles developed in an octahedral structure with agglomeration [32]. Agglomeration is confirmed for particles of these sizes because the surface energy is significant due to the huge surface to volume
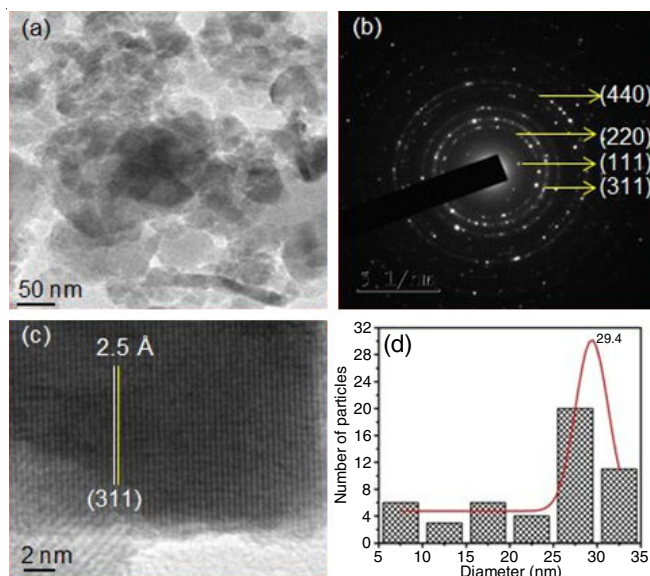

Fig. 6. Microstructural information of NCTAB sample; (a) TEM image, (b) corresponding SAED pattern, (c) HR-TEM image of (311) lattice plane and (d) particle size distribution plot

ratio. Agglomeration and their distribution are very complicated due to the magnetic property of capping agent-assisted nickel ferrite nanoparticles. The particle size distribution acquired from the TEM image is given as a histogram, with an average particle size of 29.4 nm. The formation of a dense microstructure is consistent with the low relative density values measured.

The selected area diffraction pattern displays continuous rings around a sharp spot, showing the polycrystalline nature of the synthesized samples. Each sample has a random orientation of crystalline grains. Additionally, it can be well indexed to (222), (311), (220), (222), and (111) Miller's planes of the face-centered cubic spinel structure, which is reliable with XRD performance [33]. The d-spacing measured from the diffraction rings of the SAED pattern is 2.39 Å, 2.51 Å, 2.79 Å, 2.41 Å, and 4.82 Å, correspond to (222), (311), (220), (222) and (111) planes of NPEG and NCTAB samples, respectively [34]. Thus, the TEM analysis clearly shows that the capping agent plays a vital role in determining the size of the magnetic nanoparticles which is in close agreement with the previous work [23].

The elemental characterization of $NiFe_2O_4$ nanoparticles has been analyzed by energy dispersive X-ray spectrum analysis and the results are summarized in Table-2. An EDS spectrum was recorded for all the samples, but the typical EDS spectrum of NOA sample only is displayed in Fig. 7. The spectrum confirms the presence of Ni^{2+}, Fe^{2+} and O^{2+} in the synthesized $NiFe_2O_4$ sample. There are no other impurity elements present, which shows the good quality of the synthesized sample.

The magnetic properties of ferrite nanomaterials depend on the chemical composition, particle size and the distribution of cations in tetrahedral A-sites and octahedral B-sites. Based on the distribution of cations, they can exhibit ferromagnetic, paramagnetic, antiferromagnetic or superparamagnetic properties. Generally, the particle size and chemical composition play a key role in determining the magnetic property of the spinel ferrite nanoparticles [35]. In present study, the magneti-

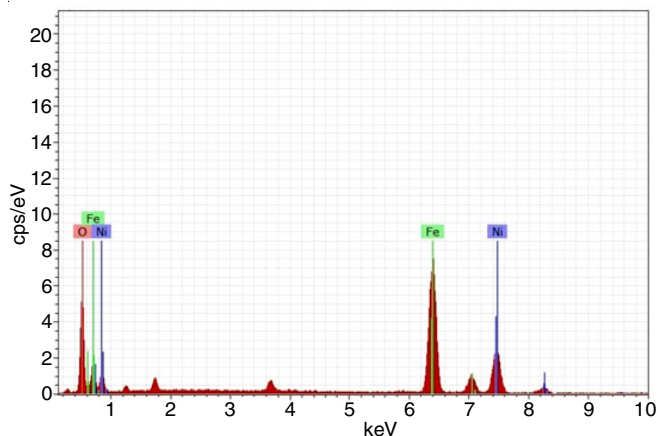| Chemical composition	Elements in (wt%)			Elements in (at%)			Total (%)
	Ni	Fe	O	Ni	Fe	O	
NSF	12.24	23.22	64.54	4.48	8.90	86.60	100
NPEG	13.84	26.79	59.37	5.33	10.84	83.83	100
NCTAB	17.91	35.97	46.12	7.96	16.81	75.23	100
NPVA	12.22	23.87	63.90	4.50	9.23	86.27	100
NOA	10.14	20.24	69.52	3.54	7.43	89.03	100

TABLE-2
EDS DATA OF CAPPING AGENTS ASSISTED $NiFe_2O_4$ NANOPARTICLES

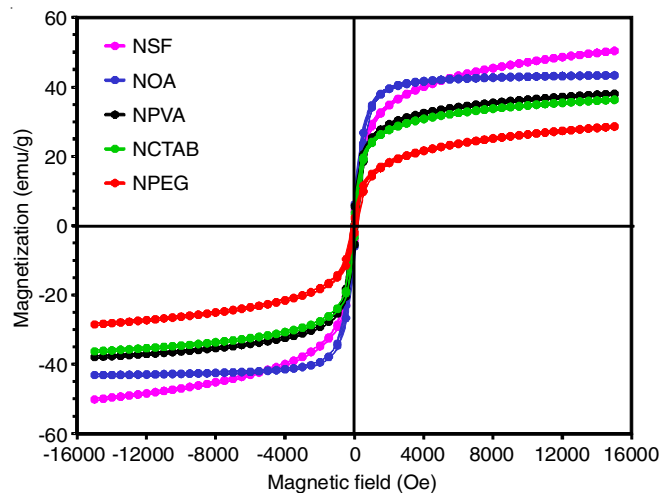Fig. 7. EDS pattern of PEG coated $NiFe_2O_4$ (NOA) sample

Fig. 8. Field dependent magnetization M(H) curves of NPEG, NCTAB, NSF, NPVA and NOA ferrite nanoparticles prepared by means of different capping agents

zation *versus* magnetic field curve (M-H) of prepared $NiFe_2O_4$ nanoparticles was recorded at room temperature using a vibrating sample magnetometer (VSM) in the magnetic field range from +16 to -16 KOe.

A typical M-H curves of the nickel ferrite samples without and with different capping agents are displayed in Fig. 8. The calculated magnetic parameters such as coercive field (H_c), saturation magnetization (M_s), remanent magnetization (M_r), squareness ratio (M_r/M_s), magnetic anisotropy constant (K), and magnetic moment (μ_B^e) determined from the M-H loops are listed in Table-3. It is known that the magnetic properties of the particles strongly depend on the grain size, porosity, and exchange interaction due to cation distribution, magneto crystalline anisotropy energy. In particular, magneto crystalline anisotropy energy has a significant influence on the shape and size of the hysteresis loop [36]. The bulk $NiFe_2O_4$ is a familiar inverse spinel with the Ni ion occupying the octahedral B site with structure $(Fe_{1-i}^{3+})_A[Ni_i^{2+}Fe_{1+i}^{2+}]_B$ while at the nanoscale, $NiFe_2O_4$ crystalizes in mixed spinel structure in which Ni^{2+} ions occupying both A and B-sites, *i.e.* $(Ni_{1-i}^{2+}Fe_i^{3+})_A[Ni_i^{2+}Fe_{2-i}^{3+}]_B$.

Referring to M-H curves, it is clear that the capping agent highly influences the magnetic behaviour of nickel ferrite nanoparticles. All the samples exhibit typical superparamagnetic behavior with an "S" shape curve with some magnetic saturation (M_s), magnetic remanence (M_r) and negligible coercivity (H_c). However, the curves appear to saturate, but they do not, except for the NPVA sample, under the applied fields, even to the maximum value of ±16 KOe. It is renowned that at the beginning of an applied field, the magnetic domain reorients, resulting in the magnetization increasing rapidly. After that due to the spin rotation, the magnetization gets slow and finally saturated. The saturation magnetization (M_s) of the samples has been evaluated using the extrapolation of magnetization (M) *versus* the inverse of the applied magnetic field (1/H). Analysis of M-H curves infers that different capping agents regulate the rate of growth of nanoparticles in different ways thereby regulating the crystallite sizes that directly affect the M-H curves. As far as the nano-$NiFe_2O_4$ is concerned, it assumes in mixed spinel structure, where the Ni^{2+} ions occupy B-site as well as A-site; therefore, a few Fe^{3+} ions migrate from B-site to A-site. The saturation magnetization of NOA and NPVA samples is 50.3 emu/g and 43.3 emu/g, respectively. Then the sample synthesized without surfactant (NSF) shows a satur-

TABLE-3
MAGNETIC PARAMETERS OF CAPPING AGENTS ASSISTED $NiFe_2O_4$ NANOPARTICLES

Sample	Particle size (D_{TEM}) (nm)	M_r (emu/g)	M_s (emu/g)	Coercivity H_c (Oe)	SQR= M_r/M_s	K_1 (× 10⁵ erg/ cm³)
NPEG	18.7	2.19	28.6	76	0.077	2.174
NCTAB	25.7	3.44	36.3	93	0.095	3.376
NSF	29.4	5.49	38.1	95	0.144	3.620
NPVA	35.0	6.07	43.3	92	0.140	3.984
NOA	50.9	4.14	50.3	82	0.082	4.125

ation magnetization of 38.1 emu/g, which is slightly greater than the saturation magnetization of sample NCTAB (36.3 emu/g). Similarly, the saturation magnetization of an NPEG sample is found to be 28.6 emu/g, which is much lower than the saturation magnetization of other samples. The maximum value of M_s reported in this particular work is 50.3 emu/g, which is comparably lower than that of saturation magnetization of bulk $NiFe_2O_4$ nanoparticles (55 emu/g) [37], 57.6 emu/g (2.417 μ_B) prepared by hydrothermal technique [38], 70.12 emu/g using the co-precipitation route and higher than the report of 44.7 emu/g by George *et al.* [39]. This low value of M_s is mainly due to the increase in the spin canting impact, with a particle size of nanometer range. The cation distribution among tetrahedral (A) and octahedral (B) sites and the crystallite size are also the reasons for the low value of saturation magnetization in the nano $NiFe_2O_4$ particles. Due to the difference in the stability of interaction and the presence of magnetic defect on the surface of the nanoparticles, the spin canting effect affects the magnetic properties of the particles. The spin canting effect is more predominant for smaller particles due to capping agents on the surface, consequently reducing the saturation magnetization of the smaller $NiFe_2O_4$ nanoparticles. A reduction in M_r value with the different capping agents suggests that $NiFe_2O_4$ nanoparticles synthesized using different capping agents can be used for data storage applications.

The squareness ratio, defined as the ratio of retentivity to saturation magnetization (M_r/M_s), measures how square the hysteresis loop is. This squareness ratio is a characteristic parameter of ferromagnetic materials and essential for their applications. It should be very small, possibly zero for magnetic fluids and large enough for memory devices. Therefore, superparamagnetic and single domain particles are mixtures of particles in this size range. The average crystalline sizes indicate the presence of larger single domain particles. Samples with a low squareness ratio of 0.1 suggest that they can be used for magnetic fluids [40].

The anisotropy symmetry of magnetite is cubic. This shows that the shape anisotropy of the nanorods governs the M-H loop. The magnetic anisotropic constant 'K' was calculated using the following formula:

$$K = \frac{H_c M_s}{0.64}$$

where M_s is saturation magnetization and H_c is the coercivity. The obtained "K" values of oleic acid and PVA capped $NiFe_2O_4$ values are high compared to other capping agent assisted $NiFe_2O_4$ samples.

Conclusion

The $NiFe_2O_4$ nanoparticles were successfully synthesized by the chemical precipitation method without and with different surfactants such as PEG, PVA, CTAB and oliec acid (OA). The synthesized samples were studied for their structural, optical, and magnetic properties. It has been observed that all these properties were influenced by the surfactants. The XRD analysis concluded that all the samples are polycrystallite and also have a cubic spinel structure. The average crystallite size and lattice constant varies for different surfactants from 19.5 to 54 nm

and 8.3623 to 8.3442 Å, respectively. The formation of ferrite nanoparticles was confirmed by the appearance of two absorption bands roughly at 598 and 452 cm⁻¹ in the FTIR spectra. The UV-visible absorption spectra indicated that the energy gap of oleic acid capped $NiFe_2O_4$ sample is 3.44 eV while for the surfactant free sample is 3.10 eV. The TEM result concludes that $NiFe_2O_4$ nanoparticles are sensitive to the studied surfactants. Moreover, VSM analysis concludes that use of surfactant increases the saturation magnetization of nanoferrites samples. On the other hand, use of CTAB reduces the coercivity to a very small level of 76 Oe. Samples exhibit nearly zero remanence and zero coercivity suggesting the super paramagnetic behaviour of the nanocrystalline nickel ferrite samples. Thus, it is concluded that capping agents plays an important role in determining the particle size. Depending upon the particle size of interest, one may select the suitable capping agent.

CONFLICT OF INTEREST

The authors declare that there is no conflict of interests regarding the publication of this article.

REFERENCES

1. A.A. Ati, Z. Othaman and A. Samavati, *J. Mol. Struct.*, **1052**, 177 (2013); https://doi.org/10.1016/j.molstruc.2013.08.040
2. S.K.E. Islam and P. Sharma, *J. Nano- Electron. Phys.*, **6**, 01008 (2014).
3. K. Nejati and R. Zabihi, *Chem. Cent. J.*, **6**, 23 (2012); https://doi.org/10.1186/1752-153X-6-23
4. M.M.L. Sonia, S. Anand, V.M. Vinosel, M.S. Janifer, S. Pauline and A. Manikandan, *J. Magn. Magn. Mater.*, **466**, 238 (2018); https://doi.org/10.1016/j.jmmm.2018.07.017
5. X. Lasheras, M. Insausti, I.G.D. Muro, E. Garaio, F. Plazaola, M. Moros, L.D. Matleis, J.M. De la Fueta and L. Lezama, *J. Phys. Chem. C*, **120**, 3492 (2016); https://doi.org/10.1021/acs.jpcc.5b10216
6. Y. Shi, J. Ding and H. Yin, *J. Alloys Compd.*, **308**, 290 (2000); https://doi.org/10.1016/S0925-8388(00)00921-X
7. C.N. Chinnasamy, A. Narayanasamy, N. Ponpandian, R.J. Joseyphus, B. Jeyadevan, K. Tohji and K. Chattopadhyay, *J. Magn. Magn. Mater.*, **238**, 281 (2002); https://doi.org/10.1016/S0304-8853(01)00928-3
8. K. Maaz, S. Karim, A. Mumtaz, S.K. Hasanain, J. Liu and J.L. Duan, *J. Magn. Magn. Mater.*, **321**, 1838 (2009); https://doi.org/10.1016/j.jmmm.2008.11.098
9. C.M. Phan and H.M. Nguyen, *J. Phys. Chem. A*, **121**, 3213 (2017); https://doi.org/10.1021/acs.jpca.7b02186
10. A. Baykal, N. Kasapoglu, Y. Köseoglu, M.S. Toprak and H. Bayrakdar, **464**, 514 (2008); https://doi.org/10.1016/j.jallcom.2007.10.041
11. M.G. Hasab, S.A.S. Ebrahimi and A. Badiei, *J. Eur. Ceram. Soc.*, **27**, 3637 (2007); https://doi.org/10.1016/j.jeurceramsoc.2007.02.004
12. M.M.L. Sonia, S. Anand, S. Blessi, S. Pauline and A. Manikandan, *Ceram. Int.*, **44**, 22068 (2018); https://doi.org/10.1016/j.ceramint.2018.08.317
13. P. Sivakumar, R. Ramesh, A. Ramanand, C. Muthamizhchelvan and S. Ponnusamy, *Mater. Res. Bull.*, **46**, 2208 (2011); https://doi.org/10.1016/j.materresbull.2011.09.009

14. A. Baykal, N. Kasapoglu, Z. Durmus, H. Kavas, M.S. Toprak and Y. Koseoglu, *Turk. J. Chem.*, **33**, 33 (2009).

15. S. Asiri, M. Sertkol, H. Gungunes, M. Amir, A.A. Manikandan, I. Ercan and A. Baykal, *J. Inorg. Organomet. Polym. Mater.*, **28**, 1587 (2018); https://doi.org/10.1007/s10904-018-0813-z

16. P. Iranmanesh, S. Tabatabai Yazdi, M. Mehran and S. Saeednia, *J. Magn. Magn. Mater.*, **449**, 172 (2018); https://doi.org/10.1016/j.jmmm.2017.10.040

17. P. Priyadharshini and K. Pushpanathan, *Surf. Rev. Lett.*, **28**, 2150052 (2021); https://doi.org/10.1142/S0218625X21500529

18. S. Joshi, M. Kumar, S. Chhoker, G. Srivastava, M. Jewariya and V.N. Singh, *J. Mol. Struct.*, **1076**, 55 (2014); https://doi.org/10.1016/j.molstruc.2014.07.048

19. S. Jain, J. Parashar and R. Kurchania, *Int. Nano Lett.*, **3**, 1 (2013); https://doi.org/10.1186/2228-5326-3-1

20. A.L. Patterson, *Phys. Rev.*, **56**, 978 (1939); https://doi.org/10.1103/PhysRev.56.978

21. A. Baykal, N. Kasapoglu, Y. Köseoglu, M.S. Toprak and H. Bayrakdar, *J. Alloys Compd.*, **464**, 514 (2008); https://doi.org/10.1016/j.jallcom.2007.10.041

22. E.I. Naik, H.S. Bhojya Naik, R. Viswanath, I.K. Suresh Gowda and B.R. Kirthan, *Mater. Sci. Technol.*, **4**, 23 (2021); https://doi.org/10.1016/j.mset.2020.12.007

23. N.A.S. Nogueira, V.H.S. Utuni, Y.C. Silva, P.K. Kiyohara, I.F. Vasconcelos, M.A.R. Miranda and J.M. Sasaki, *Mater. Chem. Phys.*, **163**, 402 (2015); https://doi.org/10.1016/j.matchemphys.2015.07.057

24. A. Ahlawat, V.G. Sathe, V.R. Reddy and A. Gupta, *J. Magn. Magn. Mater.*, **323**, 2049 (2011); https://doi.org/10.1016/j.jmmm.2011.03.017

25. A.A. Khan, M. Javed, A. Rauf Khan, Y. Iqbal, A. Majeed, S.Z. Hussain and S.K. Durrani, *Mater. Sci. Pol.*, **35**, 58 (2017); https://doi.org/10.1515/msp-2017-0006

26. R.D. Raland and J.P. Borah, *Adv. Sci. Eng. Med.*, **8**, 386 (2016); https://doi.org/10.1166/asem.2016.1871

27. L. Zhang, R. He and H.C. Gu. *Appl. Surf. Sci.*, **253**, 2611 (2006); https://doi.org/10.1016/j.apsusc.2006.05.023

28. P. Sivakumar, R. Ramesh, A. Ramanand, C. Muthamizhchelvan and S. Ponnusamy, *J. Alloys Compd.*, **537**, 203 (2012); https://doi.org/10.1016/j.jallcom.2012.05.067

29. Z. Yuan, W. You, J. Jia and L. Zhang, *Chin. Phys. Lett.*, **15**, 535 (1998); https://doi.org/10.1088/0256-307X/15/7/024

30. S. Rahman, K. Nadeem, M. Anis-ur-Rehman, M. Mumtaz, S. Naeem and I. Letofsky-Papst, *Ceram. Int.*, **39**, 5235 (2013); https://doi.org/10.1016/j.ceramint.2012.12.023

31. P. Chand, S. Vaish and P. Kumar, *Physica B*, **524**, 53 (2017); https://doi.org/10.1016/j.physb.2017.08.060

32. D.K. Dinkar, B. Das, R. Gopalan and B.S. Dehiya, *Mater. Chem. Phys.*, **218**, 70 (2018); https://doi.org/10.1016/j.matchemphys.2018.07.020

33. M. Venkatesh, G.S. Kumar, S. Viji, S. Karthi and E.K. Girija, *Mod. Electron. Mater.*, **2**, 74 (2016); https://doi.org/10.1016/j.moem.2016.10.003

34. R. Rameshbabu, R. Ramesh, S. Kanagesan, A. Karthigeyan and S. Ponnusamy, *J. Mater. Sci. Mater. Electron.*, **24**, 4279 (2013); https://doi.org/10.1007/s10854-013-1397-6

35. A. Manikandan, M. Durka and S.A. Antony, *J. Supercond. Nov. Magn.*, **28**, 2047 (2015); https://doi.org/10.1007/s10948-015-2987-8

36. M. Aliahmad, M. Noori, N.H. Kargan and M. Sargazi, *Phys. Sci. Int. J.*, **8**, 854 (2013); https://doi.org/10.5897/IJPS11.517

37. A.C.F.M. Costa, V.J. Silva, D.R. Cornejo, M.R. Morelli, R.H.G.A. Kiminami and L. Gama, *J. Magn. Magn. Mater.*, **320**, e370 (2017); https://doi.org/10.1016/j.jmmm.2008.02.159

38. K.C. Babu Naidu and W. Madhuri, *Bull. Mater. Sci.*, **40**, 417 (2017); https://doi.org/10.1007/s12034-017-1374-4

39. M. George, A. Mary John, S.S. Nair, P.A. Joy and M.R. Anantharaman, *J. Magn. Magn. Mater.*, **302**, 190 (2006); https://doi.org/10.1016/j.jmmm.2005.08.029

40. A.E. Berkowitz and W.J. Schuele, *J. Appl. Phys.*, **30**, S134 (1959); https://doi.org/10.1063/1.2185853